frontiers in Earth Science

ORIGINAL RESEARCH
published: 10 August 2021
doi: 10.3389/feart.2021.700878

Multiscale Causes of Persistent Heavy Rainfall in the Meiyu Period over the Middle and Lower Reaches of the Yangtze River

Yicong Xia, Qian Huang, Suxiang Yao and Tianle Sun*

Key Laboratory of Meteorological Disaster of Ministry of Education/Joint International Research Laboratory of Climate and Environment Change/Collaborative Innovation Center on Forecast and Evaluation of Meteorological Disasters, Nanjing University of Information Science and Technology, Nanjing, China

Based on observation data supplied by the Chinese Meteorological Administration (CMA) and reanalysis datasets provided by the ECMWF, the multiscale causes of persistent heavy rainfall events (PHREs) that occurred from 1979 to 2018 during Meiyu periods over the middle and lower reaches of the Yangtze River (MLYR) are investigated. During Meiyu periods, precipitation shows obvious interannual variabilities. In PHRE years, the contribution rate of persistent heavy rainfall to the total precipitation is approximately 57%. Precipitation also shows significant synoptic-scale (less than 10 days) characteristics. Through the quantitative diagnosis of interactions among background-scale (greater than 30 days), quasi-biweekly-scale (10–30-days), and synoptic-scale variables, the possible causes of PHREs are explored. The results reveal that the difference in precipitation intensity between PHRE years and non-PHRE years is determined by the background water vapor, background wind and synoptic-scale wind conditions. In PHRE years, the prevailing background southwesterly winds from lower latitudes provide more background water vapor, and more mean kinetic energy is converted to perturbation energy. Moreover, the active synoptic-scale oscillations from higher latitudes and the convergence of Rossby wave disturbance energy over the MLYR could also cause the occurrence and maintenance of PHREs during Meiyu periods. The multiscale causes and corresponding circulation patterns in 2020 PHREs are similar to PHREs years.

Keywords: middle and lower reaches of the yangtze river (MLYR), meiyu precipitation, multiscale diagnosis, persistent heavy rainfall events (PHREs), wave activity fluxes

OPEN ACCESS

Edited by:
Diandong Ren,
Curtin University, Australia

Reviewed by:
Chujie Gao,
Hohai University, China
Danqing Huang,
Nanjing Normal University, China

****Correspondence:***
Qian Huang
huangq@nuist.edu.cn

Specialty section:
This article was submitted to Interdisciplinary Climate Studies, a section of the journal Frontiers in Earth Science

Received: *27 April 2021*
Accepted: *22 July 2021*
Published: *10 August 2021*

Citation:
Xia Y, Huang Q, Yao S and Sun T (2021) Multiscale Causes of Persistent Heavy Rainfall in the Meiyu Period over the Middle and Lower Reaches of the Yangtze River. Front. Earth Sci. 9:700878. doi: 10.3389/feart.2021.700878

INTRODUCTION

Persistent heavy rainfall events (PHREs) and the subsequent associated disasters tend to cause catastrophic losses of property, agriculture and human lives. Several extensive flooding events have been attributed to PHREs in the history of China, such as the floods that occurred in the Yangtze River basin in 1991, 1998, and 2016 (Zhu et al., 2003; Mao and Wu 2006; Shao et al., 2018); these floods were concentrated in the middle and lower reaches of the Yangtze River (MLYR) during the typical Meiyu periods (defined by the CMA). PHREs pose a daunting challenge to flood forecasting due to their suddenness, frequency, and destructiveness. Therefore, to ensure disaster prevention and mitigation strategies, there

is an urgent need to explore the causes of PHREs and improve the prediction capability for PHREs (Chen et al., 2017; Ding et al., 2020).

Meiyu is a result of interactions between the East Asian summer monsoon system and the Eurasian mid-high-latitude circulation (Ding, 2007; Zhang et al., 2018). The summer atmospheric circulation anomaly plays a critical role in the distribution and intensity of Meiyu (Yin et al., 2014). Persistent heavy rainfalls are more likely to occur when synoptic-scale and mesoscale systems recur in the same region or move along the same path under a stable circulation pattern (Ding, 1994). Additionally, rainfall forms more frequently when the Northwest Pacific Subtropical high, the South China Sea (SCS) monsoon surge, mid-high-latitude cold air and the Tibetan Plateau mesoscale convective system are in active phases at the same time (Zhang et al., 2002; Chen and Zhai, 2014a, b; Li et al., 2019). Furthermore, the sequential warm and cold Meiyu fronts regulated by the North Atlantic Oscillation (NAO) may also lead to extreme PHREs (Wang et al., 2018; Liu et al., 2020).

The intensity and extent of the water vapor transported by the East Asian monsoon also play an essential role in regulating PHREs (Zhang, 2001; Xue et al., 2003; Yuan et al., 2017). Some studies Tao and Chen (1987), Ding (1994), Simmonds et al. (1997), Jiang et al. (2008) have revealed that water vapor transportation over China in summer is dominant in the meridional direction and originates from the SCS. Based on this, further studies have shown that, during a PHRE, water vapor transport is controlled by the Somali cross-equatorial jet, by the cross-equatorial flow near the Bay of Bengal and the Indonesian archipelago, and by the Northwest Pacific Subtropical high (Chow et al., 2008; Sun et al., 2016).

It has been documented extensively in the literature that the precipitation that occurs during Meiyu periods over the MLYR is also modulated by low-frequency circulation oscillations, which have significant intraseasonal oscillation (ISO) characteristics (Lau and Li, 1984; Yang and Li, 2003; Ding and Wang, 2008; Mao et al., 2010; Yang et al., 2010; Yao et al., 2012). The low-frequency variations and propagation of circulation systems at mid-high latitudes as well as at low latitudes impact the low-frequency variations in PHREs Mao and Wu (2006), Chen et al. (2015), while higher-frequency disturbances are also closely related to regional rainfall (Huang et al., 2016; Yao and Huang, 2016). Synoptic-scale wave trains spreading southeast from high latitudes can prevent summer monsoon from advancing northward and thus serve to maintain the rainband (Wang et al., 2021). At low latitudes, synoptic-scale perturbations can also influence the intensity of precipitation by modulating the development of tropical circulation systems (Reed and Recker, 1971; Zong and Wu, 2015).

Summer precipitation in the MLYR, as represented by Meiyu, is a multiscale phenomenon with complex multiscale interactions (Weng et al., 2008; Ding et al., 2020). Recent studies have focused on the effects of East Asian summer monsoon systems on Meiyu at a single spatial or temporal scale, such as intraseasonal oscillations (Yang, 2009; Li et al., 2015; Yan et al., 2019). In contrast, few studies have been conducted to address the influencing mechanisms of multiscale interactions. To better understand the mechanism of PHREs, this study quantitatively explores the interactions among background-scale, quasi-biweekly-scale, and synoptic-scale conditions and their relationships with extreme precipitation through the diagnosis of water vapor and energy sources with the hope that the result will be helpful for precipitation predictions during Meiyu periods.

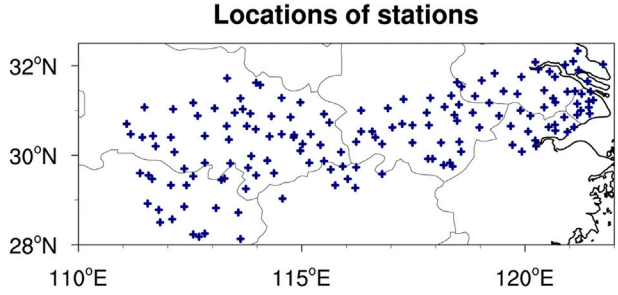

FIGURE 1 | Distribution of CMA stations over the MLYR.

DATA AND METHODS

Data

We used the ERA5 (resolution: 0.25 × 0.25°) and ERA-interim (resolution: 1 × 1) daily reanalysis datasets Dee et al. (2011) provided by the European Centre for Medium-Range Weather Forecasts (ECMWF). Among them, the ERA5 high-resolution data were used for quantitative diagnosis of the whole layer water vapor flux convergence in the MLYR, and the latter were used for the analysis of the circulation patterns, etc. These datasets include sea-level pressure (SLP), geopotential height, wind, and specific humidity data. Daily precipitation data from 2,474 stations administered by the CMA were also utilized (available online at http://data.cma.cn/). The domain of MLYR is defined as 28°–32.5°N, 110°–122°E, which includes 157 CMA stations and is shown in **Figure 1**. The period of each dataset covers 40 years (1979–2018), from June to July. Additionally, the basic monitoring data of the Meiyu (including the onset/retreat date, intensity, and precipitation) were obtained from the National Climate Center of China.

For the analysis of PHREs in 2020 Meiyu period, the CMA daily precipitation data was used to select PHREs; ERA5 (resolution: 0.25 × 0.25) datasets were used for calculating the precipitation rate; since ERA-interim data stopped updating on August 31, 2019, we used ERA5 (resolution: 1 × 1) data to explore the corresponding atmospheric activities.

Definition of PHREs During the Meiyu Period

PHRE indicators are mostly defined by the magnitude of precipitation observed by a single observation station or by the total precipitation intensity measured in the region (Bao, 2007; Chen and Zhai, 2013; Ren et al., 2013). Since the maintenance and movement of a synoptic system have important impacts on the

rainfall process, the rainband coincidence degree (C_{RB}) is considered in the definition standard (Wang et al., 2014; Sun et al., 2018). Considering both the precipitation intensity and rainband movement, the following definition criteria are used in this paper.

1) During a Meiyu period, the number of stations where the daily precipitation is greater than 50 mm should account for more than 4% of the number of effective stations. Moreover, these stations should be adjacent (the distance between each station should be less than 350 km).
2) The regional average daily precipitation should reach the sum of the climatic mean and half a standard deviation, which is greater than or equal to 8.89 mm.
3) Among the stations with daily precipitation amounts ≥50 mm, at least one station should have had ≥50 mm of precipitation on the previous day; otherwise, the overlap (C_{RB}) of the heavy-rain areas in the adjacent 2 days should exceed 20%. The C_{RB} is defined in this paper as follows:

$$\boldsymbol{C_{RB} = N_{12}/\min(N_1, N_2)} \tag{1}$$

where $\boldsymbol{N_{12}}$ represents the number of stations where the precipitation amounts of both the first and second day are larger than 11.91 mm (the sum of the climatic mean and a standard deviation); $\boldsymbol{N_1}$ represents the number of stations that satisfy this condition on the first day; and $\boldsymbol{N_2}$ represents the number of stations that satisfy this condition on the second day. If all three conditions mentioned above are met for two or more days after the target day, the whole process is considered a PHRE.

Multiscale Diagnostic Method of Precipitation

To reveal the multiscale interactions, some variables were decomposed into three terms as follows (Hsu and Li, 2011; Yao et al., 2019):

$$\boldsymbol{X = \overline{X} + X' + X''} \tag{2}$$

where $\overline{\boldsymbol{X}}$ is the background condition with a time scale greater than 30 days. A Lanczos low-frequency filter was employed to produce $\overline{\boldsymbol{X}}$. $\boldsymbol{X'}$ represents the perturbations on the 10–30-days time scale; this value is the result of the 10–30-days Butterworth bandpass filter. $\boldsymbol{X''}$ represents synoptic disturbances with a time scale less than 10 days and was extracted by applying the Lanczos high-frequency (<10 days) filter.

The water vapor flux convergence of the whole layer approximately equals the precipitation rate, which can be written as follows:

$$\boldsymbol{I} \approx -\frac{1}{\boldsymbol{g}}\int_{\boldsymbol{p_0}}^{\boldsymbol{300}} \nabla\cdot(\boldsymbol{qV})\mathbf{d}\boldsymbol{p} \tag{3}$$

where $\boldsymbol{I}$ is the precipitation rate, $\boldsymbol{g}$ is the gravitational acceleration, $\boldsymbol{p_0}$ is the surface pressure, $\boldsymbol{q}$ is the specific humidity, and $\boldsymbol{V}$ is the horizontal wind. Subsequently, the precipitation rate is decomposed into nine items, and the contribution of each item to the precipitation can be calculated quantitatively.

$$\begin{aligned}
\boldsymbol{I} &\approx -\frac{1}{\boldsymbol{g}}\int_{\boldsymbol{p_0}}^{\boldsymbol{300}} \nabla\cdot[(\overline{\boldsymbol{q}}+\overline{\boldsymbol{q}}\boldsymbol{q}'+\boldsymbol{q}'')\cdot(\overline{\boldsymbol{V}}+\boldsymbol{V}'+\boldsymbol{V}'')]\mathbf{d}\boldsymbol{p} \\
&= -\left[\frac{1}{\boldsymbol{g}}\int_{\boldsymbol{p_0}}^{\boldsymbol{300}} \nabla\cdot(\overline{\boldsymbol{q}}\,\overline{\boldsymbol{V}})\mathbf{d}p + \frac{1}{\boldsymbol{g}}\int_{\boldsymbol{p_0}}^{\boldsymbol{300}} \nabla\cdot(\overline{\boldsymbol{q}}\boldsymbol{V}')\mathbf{d}\boldsymbol{p} + \frac{1}{\boldsymbol{g}}\int_{\boldsymbol{p_0}}^{\boldsymbol{300}} \nabla\cdot(\overline{\boldsymbol{q}}\boldsymbol{V}'')\mathbf{d}\boldsymbol{p}\right. \\
&\quad + \frac{1}{\boldsymbol{g}}\int_{\boldsymbol{p_0}}^{\boldsymbol{300}} \nabla\cdot(\boldsymbol{q}'\boldsymbol{V})\mathbf{d}\boldsymbol{p} + \frac{1}{\boldsymbol{g}}\int_{\boldsymbol{p_0}}^{\boldsymbol{300}} \nabla\cdot(\boldsymbol{q}'\boldsymbol{V}')\mathbf{d}\boldsymbol{p} + \frac{1}{\boldsymbol{g}}\int_{\boldsymbol{p_0}}^{\boldsymbol{300}} \nabla\cdot(\boldsymbol{q}'\boldsymbol{V}'')\mathbf{d}\boldsymbol{p} \\
&\quad \left. + \frac{1}{\boldsymbol{g}}\int_{\boldsymbol{p_0}}^{\boldsymbol{300}} \nabla\cdot(\boldsymbol{q}''\overline{\boldsymbol{V}})\mathbf{d}\boldsymbol{p} + \frac{1}{\boldsymbol{g}}\int_{\boldsymbol{p_0}}^{\boldsymbol{300}} \nabla\cdot(\boldsymbol{q}''\boldsymbol{V}')\mathbf{d}\boldsymbol{p} + \frac{1}{\boldsymbol{g}}\int_{\boldsymbol{p_0}}^{\boldsymbol{300}} \nabla\cdot(\boldsymbol{q}''\boldsymbol{V}'')\mathbf{d}\boldsymbol{p}\right] \\
&= -\overline{\nabla\cdot\overline{\boldsymbol{q}}\overline{\boldsymbol{V}}} - \overline{\nabla\cdot\mathbf{q}\overline{\boldsymbol{V}}'} - \overline{\nabla\cdot\overline{\boldsymbol{q}}\mathbf{V}''} - \overline{\nabla\cdot\boldsymbol{q}'\overline{\boldsymbol{V}}} - \overline{\nabla\cdot\boldsymbol{q}'\boldsymbol{V}'} - \overline{\nabla\cdot\boldsymbol{q}'\boldsymbol{V}''} \\
&\quad - \overline{\nabla\cdot\boldsymbol{q}''\overline{\boldsymbol{V}}} - \overline{\nabla\cdot\boldsymbol{q}''\boldsymbol{V}'} - \overline{\nabla\cdot\boldsymbol{q}''\boldsymbol{V}''} \\
&\quad - \overline{\nabla\cdot\boldsymbol{q}''\boldsymbol{V}'} - \overline{\nabla\cdot\boldsymbol{q}''\boldsymbol{V}''}
\end{aligned} \tag{4}$$

Barotropic Energy Conversion

Based on Kosaka and Nakamura's work (2006), the energy conversion between the background and synoptic circulations is calculated as follows:

$$CK = \frac{\boldsymbol{v''^2} + \boldsymbol{u''^2}}{\boldsymbol{2}}\left(\frac{\partial\overline{\boldsymbol{u}}}{\partial\boldsymbol{x}} - \frac{\partial\overline{\boldsymbol{v}}}{\partial\boldsymbol{y}}\right) - \boldsymbol{u''v''}\left(\frac{\partial\overline{\boldsymbol{u}}}{\partial\boldsymbol{y}} + \frac{\partial\overline{\boldsymbol{v}}}{\partial\boldsymbol{x}}\right) \tag{5}$$

where $\overline{\boldsymbol{u}}$ and $\overline{\boldsymbol{v}}$ indicate the zonal and meridional components of the horizontal mean flow, respectively. In this study, we define the mean flow as the 40-years (1979–2018) climatological mean during the Meiyu periods, while $\boldsymbol{u''}$and $\boldsymbol{v''}$ indicate synoptic-scale disturbance (<10 days).

Wave Activity Flux

We calculated the wave activity flux (WAF) to depict the wave activity pattern (Takaya and Nakamura, 2001; Miao et al., 2019) using the following formula:

$$\begin{aligned}
\boldsymbol{W} = &\frac{\boldsymbol{p}\cos\varphi}{2|\boldsymbol{U}|} \\
&\cdot\left\{\begin{array}{l}
\dfrac{\boldsymbol{U}}{\boldsymbol{a^2}\cos^2\varphi}\left[\left(\dfrac{\partial\psi'}{\partial\lambda}\right)^2 - \psi'\dfrac{\partial^2\psi'}{\partial\lambda^2}\right] + \dfrac{\boldsymbol{V}}{\boldsymbol{a^2}\cos\varphi}\left[\dfrac{\partial\psi'}{\partial\lambda}\dfrac{\partial\psi'}{\partial\varphi} - \psi'\dfrac{\partial^2\psi'}{\partial\lambda\partial\varphi}\right] \\
\dfrac{\boldsymbol{U}}{\boldsymbol{a^2}\cos\varphi}\left[\dfrac{\partial\psi'}{\partial\lambda}\dfrac{\partial\psi'}{\partial\varphi} - \psi'\dfrac{\partial^2\psi'}{\partial\lambda\partial\varphi}\right] + \dfrac{\boldsymbol{V}}{\boldsymbol{a^2}}\left[\left(\dfrac{\partial\psi'}{\partial\varphi}\right)^2 - \psi'\dfrac{\partial^2\psi'}{\partial\varphi^2}\right] \\
\dfrac{\boldsymbol{f_0^2}}{\boldsymbol{N^2}}\left\{\dfrac{\boldsymbol{U}}{\boldsymbol{a}\cos\varphi}\left[\dfrac{\partial\psi'}{\partial\lambda}\dfrac{\partial\psi'}{\partial z} - \psi'\dfrac{\partial^2\psi'}{\partial\lambda\partial z}\right] + \dfrac{\boldsymbol{V}}{\boldsymbol{a}}\left[\dfrac{\partial\psi'}{\partial\varphi}\dfrac{\partial\psi'}{\partial z} - \psi'\dfrac{\partial^2\psi'}{\partial\varphi\partial z}\right]\right\}
\end{array}\right.
\end{aligned} \tag{6}$$

where ψ' is the perturbed stream function on the synoptic scale, $\boldsymbol{U}$ is the horizontal mean flow with U and V as the zonal and meridional components, respectively, f_0 is the Coriolis parameter, and N^2 represents the static stability parameter and is defined by $N^2 = -\alpha(\partial\ln\theta/\partial p)$. The term θ represents the

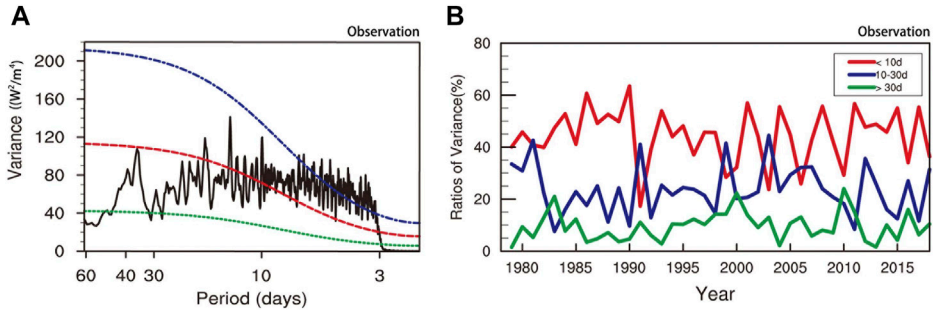

FIGURE 2 | (A) Power spectrum analysis of precipitation from June to July of 1979-2018 (units: W^2 m^{-4}). The red dashed line is the red noise spectrum, and the blue (green) dashed line indicates values above the 95% (5%) confidence level **(B)** Variance contributions of precipitation components at different time scales to precipitation anomalies (red, synoptic scale; blue, quasi-biweekly scale; green, background scale).

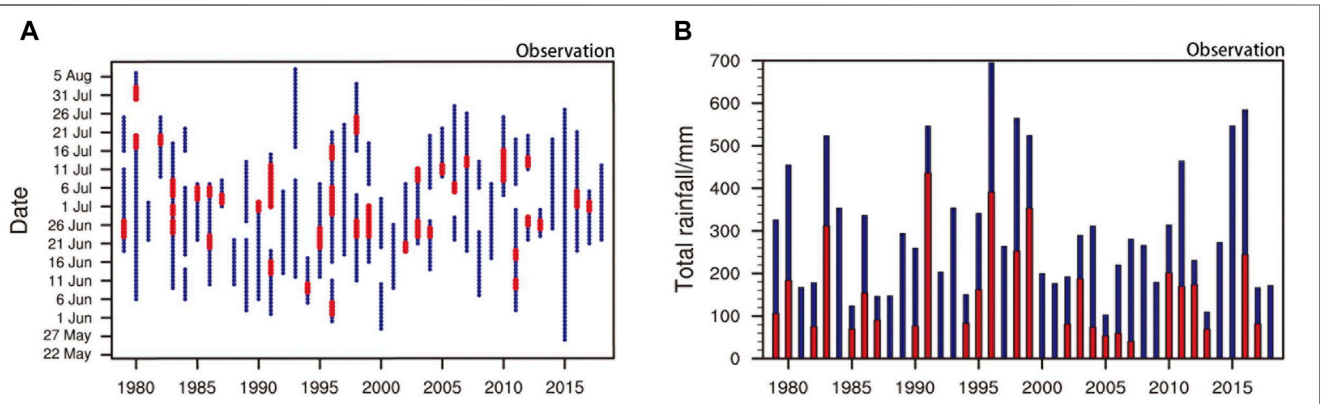

FIGURE 3 | (A) Distributions of PHREs (red marks) and typical Meiyu periods (blue marks) over the MLYR during 1979-2018 **(B)** The accumulated precipitation that occurs during PHREs (solid red bars, units: mm) and Meiyu periods (solid blue bars, units: mm).

potential temperature, and α denotes the specific volume. The WAF vector is parallel to the group velocity of the Rossby wave in the WKB (Wentzel-Kramers-Brillouin) approximation. When the WAF vectors converge, the wave energy accumulates, and this condition is conducive to enhancing the disturbance; the wave energy disperses when the WAF vectors diverge.

RESULTS

Climatic Characteristics of PHREs

The power spectrum of the 3-days running-mean daily precipitation data (**Figure 2A**) was analyzed to obtain the dominant precipitation periods during the Meiyu periods over the MLYR. The results show that the precipitation during these periods has remarkably high-frequency oscillations with periods of 3–10 days, while the second-most significant periods is 10–30 days. By calculating the contributions of the rainfall components at different scales to the precipitation anomalies, the annual mean-variance contribution of the 3–10-days component is 44% (**Figure 2B**); this value is significantly larger than those of the quasi-biweekly (10–30-days) component and the background component.

Based on the definition provided in *Definition of PHREs during the Meiyu Period*, 37PHREs that occurred during Meiyu periods were selected, with an average duration of 4.35 days. Climatically, the PHREs were concentrated in June-July, with a high incidence from mid-June to mid-July (**Figure 3A**). It is worth noting that the variation in total precipitation during the Meiyu period corresponds well to the PHREs (**Figure 3B**). The total precipitation tends to be higher in years when PHREs are frequent and persistent, such as 1983, 1991, 1996, 1998, and 1999. All these years were typical flood years in the MLYR. In addition, interannual variations in precipitation were more evident before 2000, especially in the 1990s; this is consistent with the findings of Huang et al. (2011) and Liang and Ding (2017). The observed increases in the total precipitation were mainly attributed to extreme events (Zhai et al., 1999), revealing the linkage between PHREs and flooding. For the subsequent analysis, years with PHRE precipitation amounts greater than 1.5 standard deviations of

TABLE 1 | PHRE years and non-PHRE years.

PHRE years	1980, 1983, 1991, 1996, 1998, 1999, 2003, 2010, 2016
Non-PHRE years	1981, 1984, 1988, 1989, 1992, 1993, 1997, 2000, 2001, 2008, 2009, 2014, 2015, 2018

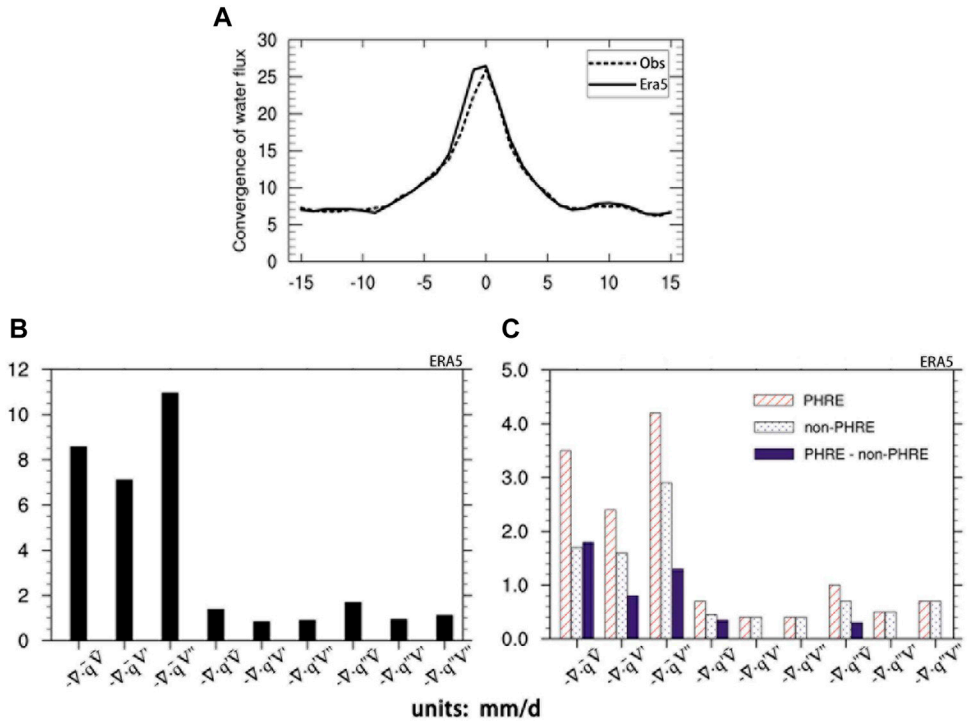

FIGURE 4 | (A) The precipitation totals calculated by the vertical integral of the vapor flux convergence and observed precipitation (dashed line) (units: mm/d) averaged over the MLYR during PHREs with durations of −15 to 15 days, for which day 0 represents all PHRE days **(B)** The nine items calculated by the vertical integral of the vapor flux convergence during PHREs (units: mm/d) **(C)** the nine items calculated in PHRE years (red slant), non-PHRE years (blue dots), and the differences between these years (solid blue bars) (units: mm/d). The horizontal axes in **Figures 4B, C** show the interactions between wind and specific humidity at different time scales, as shown in **Eqs 2**, **3**, and **4**.

the persistent heavy rainfall average are defined as PHRE years, while years without PHREs are called non-PHRE years (**Table 1**).

Multiscale Analysis of Interannual Variations in PHREs

Precipitation is the product of interactions between circulation and water vapor. Horizontal convergence and ascending motion are required when water vapor is transported from a source region to the MLYR during rainfall events. In this section, the contributions of multiscale interactions to precipitation are quantitatively diagnosed based on the method described in *Multiscale Diagnostic Method of Precipitation* while considering the differences between PHRE years and non-PHRE years.

The convergence of the whole-layer integral water vapor flux is calculated based on **Eq. 3** and then multiplied by 86,400; thus, the convergence has the same unit as the precipitation (mm/day). The lead-lag composite analysis provided in **Figure 4A** shows that the convergence is consistent with the evolution of PHREs. Therefore, we decompose the vapor flux convergence into nine items according to **Eq. 4**. This decomposition reveals that the background water vapor and synoptic-scale disturbances contribute the most to PHREs (**Figure 4B**). Similarly, by decomposing the Meiyu precipitation, it is determined that the precipitation produced by background water vapor and synoptic-scale disturbances contributes the most in terms of both PHRE years and non-PHRE years (**Figure 4C**). Notably, both PHREs and their interannual variabilities mainly depend on $-\overline{\nabla \cdot \bar{q}\bar{V}}$ and. $-\overline{\nabla \cdot \bar{q}V''}$. Hence, we consider that persistent heavy rainfall is closely related to the background water vapor field, background wind field and synoptic-scale wind field. **Figure 5** shows the composites of background fields and synoptic-scale fields for PHREs to illustrate the impact of the aforementioned two items

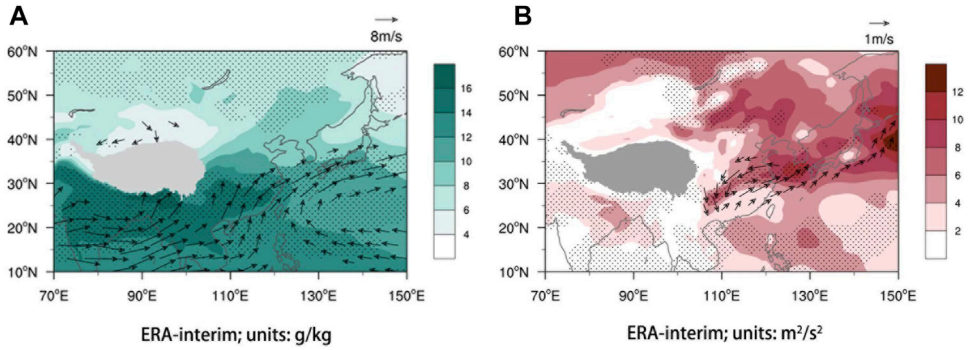

FIGURE 5 | (A) The distributions of background specific humidity at 850 hPa (shadings; units: g/kg; dots are the areas with statistical significance exceeding the 95% level) and background wind (vectors; unit: m/s; only locally statistically significant (>95%) vectors are shown) and **(B)** the disturbance kinetic energy at 850 hPa (shadings; units: $m^2\ s^{-2}$; dots are the areas with statistical significance exceeding the 95% level) and $\boldsymbol{V''}$ (vectors; units: m/s; only locally statistically significant (>95%) vectors are shown) during PHREs.

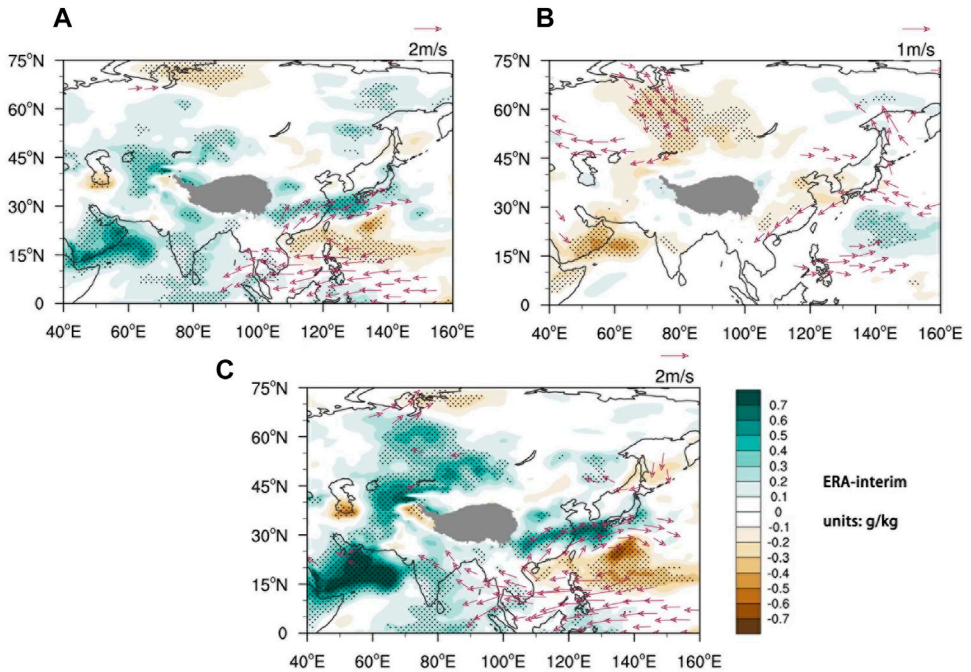

FIGURE 6 | The distributions of background specific humidity at 850 hPa (shadings; units: g/kg; dots are the areas with statistical significance exceeding the 95% level) and background wind (vectors; units: m/s; only locally statistically significant (>95%) vectors are shown) anomalies in **(A)** PHRE years and in **(B)** non-PHRE years as well as **(C)** the differences between the two during Meiyu periods.

on the precipitation. From the distributions of the background water vapor and background wind (**Figure 5A**), it is found that the MLYR is located in the area where abundant water vapor is available. Also, the prevalent southwest background winds conveying water vapor from the Bay of Bengal to the region, providing a favorable environment for the occurrence of extreme events. To explore the characteristics of the synoptic-scale field, **Figure 5B** presents the distributions of the disturbance kinetic energy and synoptic-scale wind field. It can be clearly seen that the disturbance energy is mainly concentrated over the MLYR, indicating vigorous synoptic-scale disturbances exists over this region. Meanwhile, there is a pronounced synoptic-scale cyclone above the MLYR, which is conducive to the horizontal convergence and ascending motion of water vapor. Therefore, the background fields and synoptic-scale fields are favorable for enhancing the probability of PHREs occurrence.

From what has been discussed above, it seems to verify that the background fields and synoptic-scale disturbances play an

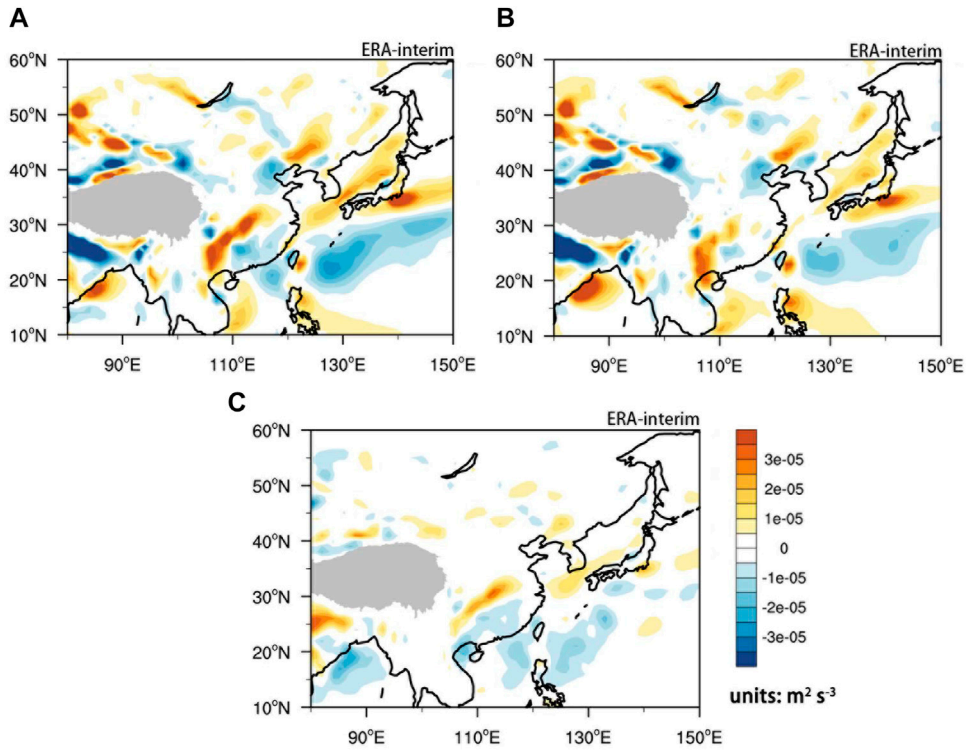

FIGURE 7 | The distributions of barotropic energy conversion at 850 hPa in **(A)** PHRE years **(B)** non-PHRE years, and **(C)** the differences between the two during the Meiyu period (units: $m^2\ s^{-3}$).

essential role in the PHREs in MLYR. Then, we will discuss whether they also affect the interannual variabilities of PHREs (showed in **Figure 4C**).

By applying a composite analysis, the different spatial features of the background water vapor and background wind fields between PHRE years and non-PHRE years were further analyzed (**Figure 6**). In PHRE years, the southwesterly wind anomaly of the anomalous anticyclonic activity induces ample water vapor transport from the SCS to the MLYR (**Figures 6A, C**), providing a warm and wet environment for extreme precipitation. This suggests that the background water vapor and circulation conditions appear to be more favorable in PHRE years. Opposite characteristics are seen in non-PHRE years (**Figure 6B**), compared to PHRE years, the most remarkable feature is that the negative water vapor anomaly in the MLYR is coupled with a cyclonic circulation anomaly over the western Pacific. This indicates that the background water vapor in non-PHRE years is insufficient to induce rainfall, also, the background circulation hinders the water vapor transport from lower latitudes.

Eq. 5 is used to diagnose the conversion between the mean kinetic energy and synoptic-scale perturbation energy. A positive (negative) CK term represents that the synoptic-scale winds gain (loss) energy from the mean flows. **Figures 7A, B** show that the CK term is positive along the MLYR in both PHRE years and non-PHRE years, indicating that low-level mean flows convert kinetic energy to synoptic-scale perturbation energy, thus promoting the occurrence and development of circulation disturbances in this region. However, the mean flows give more kinetic energy to perturbation energy during PHRE years (**Figure 7C**), therefore, the energy conversion is comparatively vigorous in PHRE years, which favors the intensification of synoptic-scale disturbances that associated with PHREs. Thus, assuming consistent background water vapor and circulation conditions, the increase in available energy gained from the mean flows in PHRE years may be prone to induce PHREs.

In the above analysis, the differences in energy conversion were discussed; what about the differences in the propagation of synoptic-scale disturbances? In addition to using the CK term to describe the perturbations, we take the center of the MLYR (30°N, 115°E) as the base point and use the one-point lag correlation method (**Figure 8**) to describe the propagation patterns of synoptic-scale disturbances. As determined from the distributions of the correlation coefficients, the synoptic-scale fluctuations are mainly located in the subtropical region and migrate through North Africa and the Tibetan Plateau, before then arriving in the MLYR region and finally moving toward the Northwest Pacific. For PHRE years shown in **Figure 8A–E**, it is worth noting that from day −2 to day 0, the positive center gradually strengthens and moves eastward, reaching a maximum over the MLYR, and then slowly moves into the sea. This fluctuation widely covers the mid-latitudes, with its pattern remaining relatively intact until +2 days, reflecting the activity

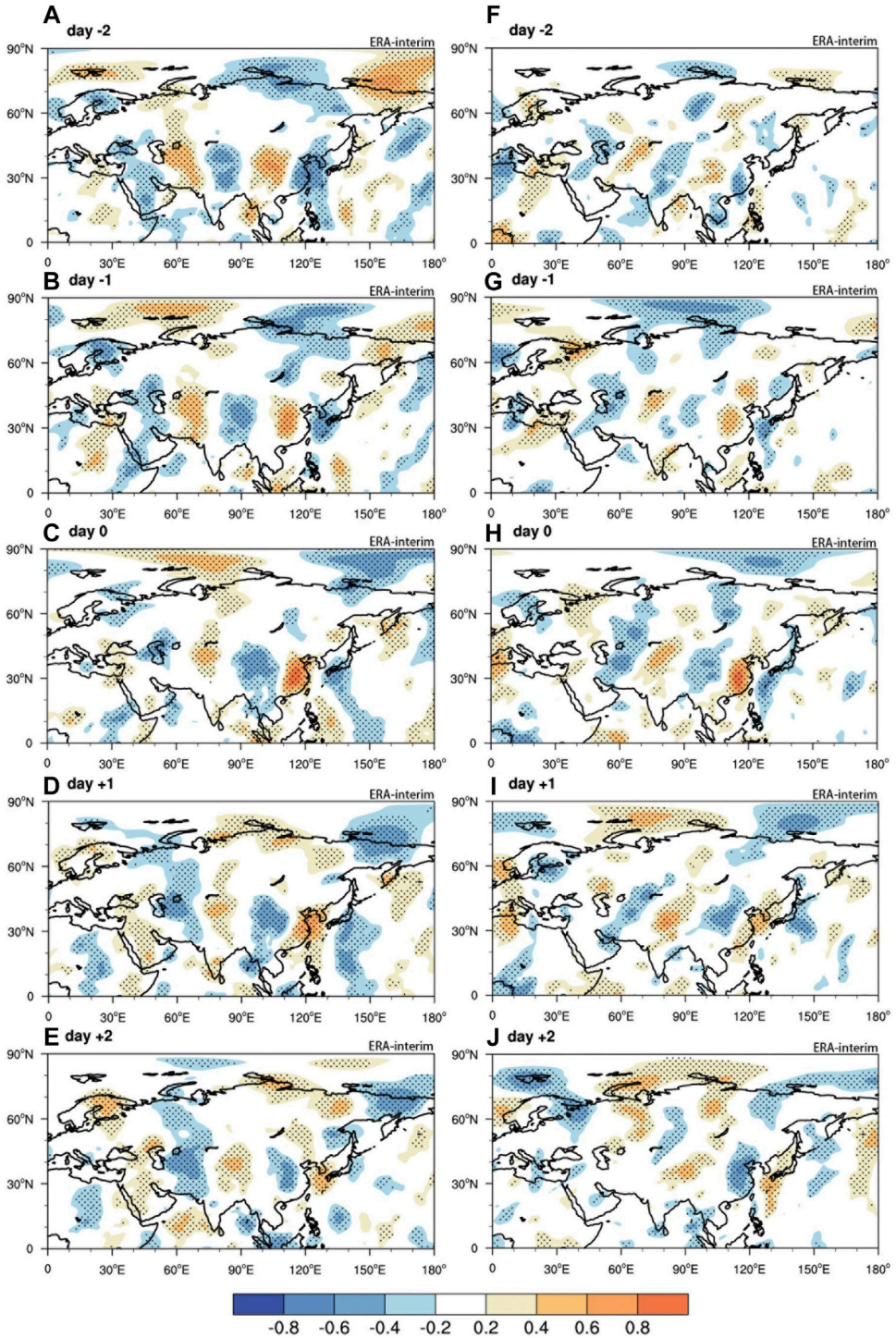

FIGURE 8 | One-point lag correlation of 300 hPa v'' at the base point (30°N, 115°E) from day −2 to day +2 during Meiyu periods in PHRE years **(A–E)** and non-PHRE years **(F–J)**. Areas with absolute values less than 0.2 are omitted. The dots show the areas with Monte Carlo (Ebisuzaki, 1996) significances exceeding the 95% level.

and durability of synoptic-scale disturbances. In non-PHRE years (**Figure 8F–J**), although the wave train also obviously propagates eastward, its pattern is unclear, and the duration of the upstream wave is relatively short. Overall, the propagation of synoptic-scale disturbances differs significantly between PHRE years and non-PHRE years. The prolonged stagnation of disturbances in PHRE years may lead to the extreme maintenance of precipitation in the MLYR.

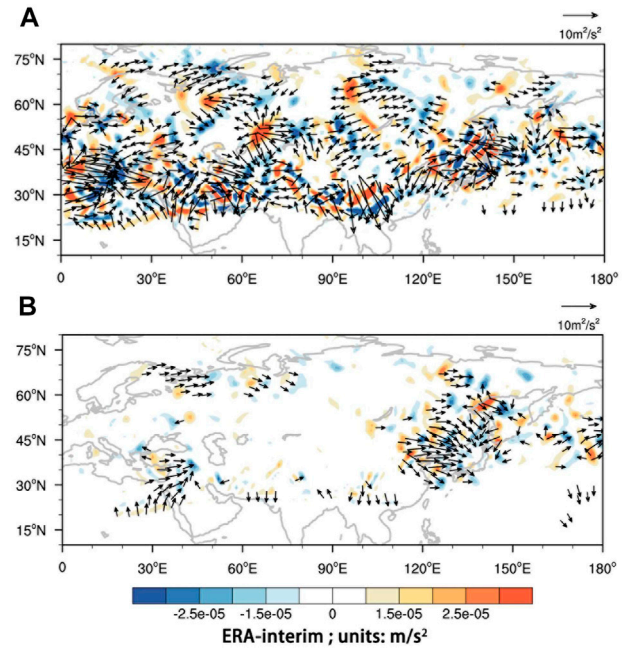

FIGURE 9 | The distributions of the WAF at 300 hPa (vectors; units: $m^2\ s^{-2}$) and the WAF divergence (shadings; units: $m\ s^{-2}$) during Meiyu periods in **(A)** PHRE years and **(B)** non-PHRE years.

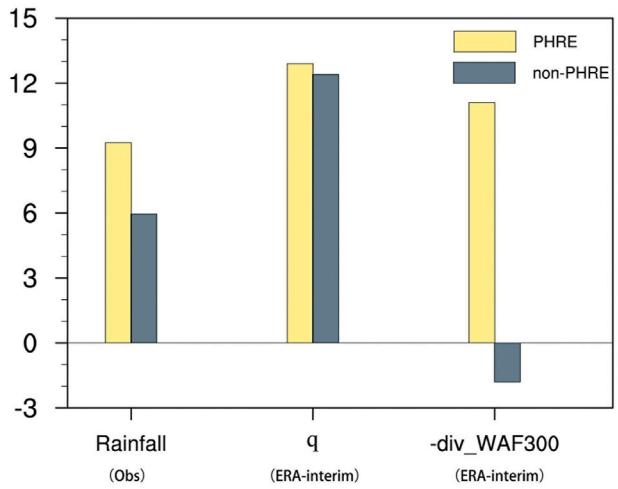

FIGURE 10 | Precipitation (units: mm/d), background specific humidity at 850 hPa (units: g/kg), and divergence of the WAF at 300 hPa (units: $10^{-6}\ m/s^2$) averaged over the MLYR. The yellow bars and blue bars denote PHRE years and non-PHRE years, respectively.

Numerous studies have shown that precipitation anomalies in the MLYR are closely related to the southeastward-propagating mid-latitude wave train (MLWT) (Fujinami and Yasunari, 2009; Liu et al., 2020; Ouyang and Liu, 2020). To further illustrate the role of high-frequency wave train in the anomalous circulation associated with PHREs, we calculated the wave activity flux (WAF) according to the method described in *Wave Activity Flux*. As shown, the dispersion modes of wave disturbances in PHRE years and non-PHRE years are clearly different. For PHRE years (**Figure 9A**), the wave disturbance over Eurasia is in an active state, with the convergence and dispersion centers aligned in the subtropical zone along 30°N. Wave trains originating from the northeast and northwest routes propagate simultaneously and convey synoptic-scale wave energy. The energy converges over the MLYR, and this convergence is conducive to the strengthening of synoptic-scale disturbances (Tam and Li, 2006). However, in non-PHRE years (**Figure 9B**), the wave disturbance is much weaker at mid-latitudes, with no apparent convergence or divergence in the upstream region. Moreover, a slight disturbance energy divergence exists over the MLYR.

To directly describe the relationships among background water vapor, synoptic-scale disturbances, and PHREs, the regionally averaged background specific humidity over the MLYR was selected to represent the water vapor conditions. The average convergence (divergence) of the WAF denotes the strengthening (weakening) of the synoptic-scale disturbances in this region. **Figure 10** shows composites of the variables mentioned above in PHRE years and non-PHRE years, from which we can observe the close relationship between the two variables and PHREs. Compared with non-PHRE years, water vapor is slightly increased in PHRE years. However, the wave disturbance energy accumulation over the MLYR in PHRE years is significantly stronger than that in non-PHRE years, providing favorable conditions for the occurrence and maintenance of precipitation during Meiyu periods, especially during PHREs.

Multiscale Analysis of 2020 PHREs

In 2020, the MLYR suffered a long-persisting Meiyu period. The accumulated precipitation (758.7 mm) broke its record since 1961 and caused catastrophic flooding and death in China. According to the definition in *Definition of PHREs during the Meiyu Period* , during the Meiyu period of 2020, four PHREs occurred in the MLYR (**Table 2**), and the accumulated precipitation reached 385.0 mm, accounting for approximately 51% of the total precipitation in the Meiyu period. The spectral analysis shows that the Meiyu rainfall has significant peaks at synoptic (<10 days) scales (**Figure 11A**). The peaks are significantly larger than the red-noise spectral level, suggesting that the major rainfall events in MLYR during the Meiyu period in 2020 are closely associated with the synoptic-scale disturbances.

To understand the multiscale interactions of the PHREs in the 2020 Meiyu period, we also decompose the water vapor flux convergence into nine items according to **Eq. 4** (**Figure 11B**). The results indicate that the $-\nabla\cdot\overline{\bar{q}\bar{V}}$ and $-\nabla\cdot\overline{\bar{q}V''}$ items are the main contributors of PHREs in the 2020 Meiyu period, which is consistent with the conclusions on the climatic characteristics of PHREs in *Multiscale Analysis of Interannual Variations in PHREs*. The spatial characteristics of the background water vapor, background circulation and synoptic-scale disturbances in **Figure 12** confirm the diagnostic results. Moreover, compared with the climatic features (**Figure 5**), the background

TABLE 2 | Duration of 2020 PHREs in Meiyu period.

Date	12 Jun~15 Jun	19 Jun~23 Jun	27 Jun~29 Jun	02 Jul~08 Jul
Duration	4d	5d	3d	7d

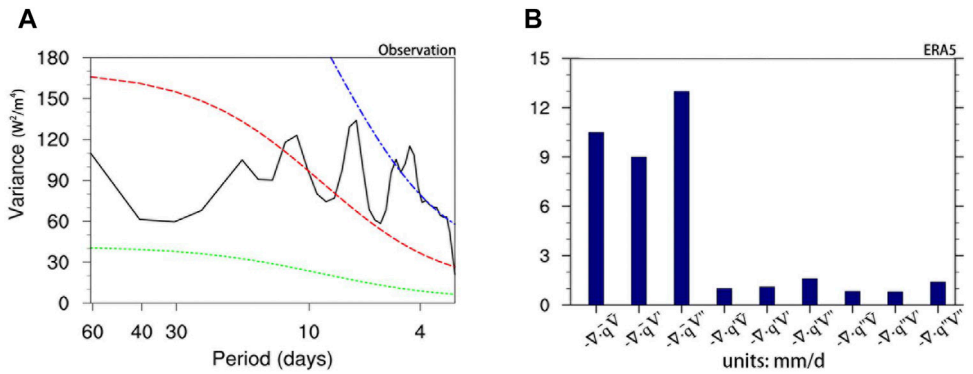

FIGURE 11 | (A) Same as **Figure 2A** but for the power spectrum analysis of precipitation from May to August of 2020 **(B)** Same as **Figure 4B** but for the 2020 PHREs.

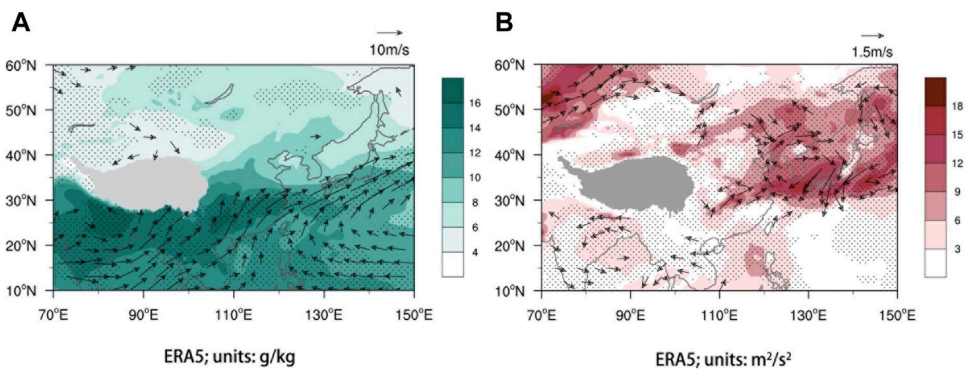

FIGURE 12 | As in **Figure 5** but for the composites of 2020 PHREs.

southwesterly flow is more prevalent and the synoptic-scale disturbance center is enhanced in 2020 PHREs.

CONCLUSION AND DISCUSSION

The present study provides a multiscale analysis of PHREs over the MLYR during Meiyu periods. In the observations, significant interannual variations occurred in precipitation in the MLYR. Persistent heavy rainfall accounted for approximately 57% of the total precipitation during Meiyu periods.

The precipitation characteristics in PHRE years (with PHRE precipitation greater than 1.5 standard deviations of the persistent heavy rainfall) and non-PHRE years were further analyzed. The results of the power spectrum analysis show that Meiyu precipitation has significant synoptic-scale characteristics (<10 days). The diagnostic analysis of the precipitation rate indicates that the interannual variations in precipitation during Meiyu periods, that is, the variability in PHREs, depends mainly on the background water vapor and circulation conditions as well as synoptic-scale disturbances.

In the lower troposphere, abundant background water vapor is accompanied by prevailing background southwesterly winds, while synoptic-scale disturbances gain available energy from the mean flow and thus serve to enhance the circulation anomalies. In the upper troposphere, synoptic-scale disturbances propagate persistently eastward over the Eurasian continent, and the wave energy converges, contributing primarily to the anomalous circulations associated with PHREs.

Similar to the climatic characteristics, the 2020 Meiyu rainfall also exhibits significant high-frequency (<10 days) oscillation, and the PHREs are mainly modulated by background fields and synoptic-scale disturbances. Moreover, their contribution to extreme precipitation is relatively more pronounced.

The above studies mainly determined the relationships between PHREs and atmospheric circulations at different time scales in the MLYR through multiscale diagnosis methods; however, there are still some shortcomings. For example, the durations of different PHREs may be long or short, and, for a 3-days rainstorm and a 7-days rainstorm, the circulation patterns may have different dominant periods. In the previous multiscale analysis, only two prominent items ($-\nabla \cdot \overline{\boldsymbol{q}}\,\overline{\boldsymbol{V}}$ and $-\overline{\nabla \cdot \overline{\boldsymbol{q}}\boldsymbol{V}''}$) were considered. However, quasi-biweekly-scale disturbances may also be important as can be seen in **Figures 2**, **4**, **12**. Therefore, in our follow-up work, we will examine the longer PHREs (e.g., >5 days) and shorter PHREs (3–5 days) separately. Also, we will diagnose the contributions of circulation at different scales, especially the quasi-biweekly-scale, in these two types of PHREs. In addition, significant interdecadal differences exist in PHREs in the MLYR, and the mechanisms behind these differences still need further discussion.

DATA AVAILABILITY STATEMENT

The raw data supporting the conclusions of this article will be made available by the authors, without undue reservation.

AUTHOR CONTRIBUTIONS

QH and YX conceived the idea, conducted the data analysis and prepared the figures. YX, SY and TS discussed the results and wrote the paper.

FUNDING

This research was funded by the National Key R&D Program of China (Grant 2018YFC1505802), the National Natural Science Foundation of China (41930969), and the Open Research Foundation of Chongqing Meteorological Bureau, China (CQM140905).

ACKNOWLEDGMENTS

We acknowledge the support from the National Key R&D Program of China (Grant 2018YFC1505802), the National Natural Science Foundation of China (41930969), and the Open Research Foundation of Chongqing Meteorological Bureau, China (CQM140905).

REFERENCES

Bao, M. (2007). The Statistical Analysis of the Persistent Heavy Rain in the Last 50 Years over China and Their Backgrounds on the Largescale Circulation. *Chin. J. Atmos. Sci.* 31, 779–792. (in Chinese).

Chen, G., Sha, W., Iwasaki, T., and Wen, Z. (2017). Diurnal Cycle of a Heavy Rainfall Corridor over East Asia. *Mon. Wea. Rev.* 145, 3365–3389. doi:10.1175/MWR-D-16-0423.1

Chen, J., Wen, Z., Wu, R., Chen, Z., and Zhao, P. (2015). Influences of Northward Propagating 25-90-day and Quasi-Biweekly Oscillations on Eastern china Summer Rainfall. *Clim. Dyn.* 45 (1/2), 105–124. doi:10.1007/s00382-014-2334-y

Chen, Y., and Zhai, P. (2013). Persistent Extreme Precipitation Events in China during 1951-2010. *Clim. Res.* 57 (2), 143–155. doi:10.3354/cr01171

Chen, Y., and Zhai, P. (2014a). Precursor Circulation Features for Persistent Extreme Precipitation in Central-Eastern China. *Weather Forecast.* 29, 226–240. doi:10.1175/waf-d-13-00065.1

Chen, Y., and Zhai, P. (2014b). Two Types of Typical Circulation Pattern for Persistent Extreme Precipitation in Central-Eastern China. *Q.J.R. Meteorol. Soc.* 140, 1467–1478. doi:10.1002/qj.2231

Chow, K. C., Tong, H.-W., and Chan, J. C. L. (2008). Water Vapor Sources Associated with the Early Summer Precipitation over china. *Clim. Dyn.* 30 (5), 497–517. doi:10.1007/s00382-007-0301-6

Dee, D. P., Uppala, S. M., Simmons, A. J., Berrisford, P., Poli, P., Kobayashi, S., et al. (2011). The ERA-Interim Reanalysis: Configuration and Performance of the Data Assimilation System. *Q.J.R. Meteorol. Soc.* 137, 553–597. doi:10.1002/qj.828

Ding, Y., Liang, P., Liu, Y., and Zhang, Y. (2020). Multiscale Variability of Meiyu and its Prediction: a New Review. *J. Geophys. Res. Atmospheres.* 125 (7), e2019JD031496. doi:10.1029/2019jd031496

Ding, Y. (1994). Monsoons over china. *Adv. Atmos. Sci.* 11 (2), 252. doi:10.1007/BF02666553

Ding, Y. (2007). The Variability of the Asian Summer Monsoon. *J. Meteorol. Soc. Jpn.* 85B, 21–54. doi:10.2151/jmsj.85b.21

Ebisuzaki, W. (1996). A Method to Estimate the Statistical Significance of a Correlation when the Data Are Serially Correlated. *J. Clim.* 10 (9), 2147–2153.

Fujinami, H., and Yasunari, T. (2009). The Effects of Midlatitude Waves over and Around the Tibetan Plateau on Submonthly Variability of the East Asian Summer Monsoon. *Mon. Wea. Rev.* 137 (7), 2286–2304. doi:10.1175/2009mwr2826.1

Hsu, P.-C., and Li, T. (2011). Interactions between Boreal Summer Intraseasonal Oscillations and Synoptic-Scale Disturbances over the Western North Pacific. Part II: Apparent Heat and Moisture Sources and Eddy Momentum Transport*. *J. Clim.* 24, 942–961. doi:10.1175/2010jcli3834.1

Huang, D., Zhu, J., and Kuang, X. (2011). Decadal Variation of Different Durations of Continuous Meiyu Precipitation and the Possible Cause. *Chin. Sci. Bull.* 56 (4), 424–431. doi:10.1007/s11434-010-4241-x

Huang, H., Wang, Y., He, J., Chen, S., and Qin, J. NUIST (2016). Impact of Synoptic Scale Wave Train on Meiyu over the Middle and Lower Reaches of Yangtze River in June. *Trans. Atmos. Sci.* 39 (1), 28–36.

Hui, Y., and Chongyin, L. (2003). The Relation between Atmospheric Intraseasonal Oscillation and Summer Severe Flood and Drought in the Changjiang-Huaihe River basin. *Adv. Atmos. Sci.* 20 (4), 540–553. doi:10.1007/BF02915497

Jiang, Z., Yang, S., He, J., Li, J., and Liang, J. (2008). Interdecadal Variations of East Asian Summer Monsoon Northward Propagation and Influences on Summer Precipitation over east china. *Meteorol. Atmos. Phys.* 100 (1-4), 101–119. doi:10.1007/s00703-008-0298-3

Kosaka, Y., and Nakamura, H. (2006). Structure and Dynamics of the Summertime pacific-japan Teleconnection Pattern. *Q.J.R. Meteorol. Soc.* 132 (619), 2009–2030. doi:10.1256/qj.05.204

Lau, K.-M., and Li, M.-T. (1984). The Monsoon of East Asia and its Global Associations-A Survey. *Bull. Amer. Meteorol. Soc.* 65 (2), 114–125. doi:10.1175/1520-0477(1984)065<0114:tmoeaa>2.0.co;2

Li, H., He, S., Fan, K., and Wang, H. (2019). Relationship between the Onset Date of the Meiyu and the South Asian Anticyclone in April and the Related Mechanisms. *Clim. Dyn.* 52, 209–226. doi:10.1007/s00382-018-4131-5

Li, J., Mao, J., and Wu, G. (2015). A Case Study of the Impact of Boreal Summer Intraseasonal Oscillations on Yangtze Rainfall. *Clim. Dyn.* 44 (9-10), 2683–2702. doi:10.1007/s00382-014-2425-9

Liang, P., and Ding, Y. (2017). The Long-Term Variation of Extreme Heavy Precipitation and its Link to Urbanization Effects in Shanghai during 1916-2014. *Adv. Atmos. Sci.* 34 (3), 321–334. doi:10.1007/s00376-016-6120-0

Liu, B., Yan, Y., Zhu, C., Ma, S., and Li, J. (2020). Record-Breaking Meiyu Rainfall Around the Yangtze River in 2020 Regulated by the Subseasonal Phase Transition of the North Atlantic Oscillation. *Geophys. Res. Lett.* 47, e2020GL090342. doi:10.1029/2020GL090342

Mao, J., Sun, Z., and Wu, G. (2010). 20-50-day Oscillation of Summer Yangtze Rainfall in Response to Intraseasonal Variations in the Subtropical High over the Western north pacific and south china Sea. *Clim. Dyn.* 34 (5), 747–761. doi:10.1007/s00382-009-0628-2

Mao, J., and Wu, G. (2006). Intraseasonal Variations of the Yangtze Rainfall and its Related Atmospheric Circulation Features during the 1991 Summer. *Clim. Dyn.* 27 (7-8), 815–830. doi:10.1007/s00382-006-0164-2

Miao, R., Wen, M., Zhang, R., and Li, L. (2019). The Influence of Wave Trains in Mid-high Latitudes on Persistent Heavy Rain during the First Rainy Season over south china. *Clim. Dyn.* 53, 2949–2968. doi:10.1007/s00382-019-04670-y

Ouyang, Y., and Liu, F. (2020). Intraseasonal Variability of Summer Monsoon Rainfall over the Lower Reaches of the Yangtze River basin. *Atmos. oceanic Sci. Lett.* 13 (4), 323–329. doi:10.1080/16742834.2020.1741322

Reed, R. J., and Recker, E. E. (1971). Structure and Properties of Synoptic-Scale Wave Disturbances in the Equatorial Western pacific. *J. Atmos. Sci.* 28 (7), 1117–1133. doi:10.1175/1520-0469(1971)028<1117:saposs>2.0.co;2

Ren, X., Yang, X.-Q., and Sun, X. (2013). Zonal Oscillation of Western Pacific Subtropical High and Subseasonal SST Variations during Yangtze Persistent Heavy Rainfall Events. *J. Clim.* 26, 8929–8946. doi:10.1175/JCLI-D-12-00861.1

Shao, X., Li, S., Liu, N., and Song, J. (2018). The Madden-Julian Oscillation during the 2016 Summer and its Possible Impact on Rainfall in China. *Int. J. Climatol* 38, 2575–2589. doi:10.1002/joc.5440

Simmonds, I., Bi, D., and Hope, P. (1997). Atmospheric Water Vapor Flux and its Association with Rainfall over China in Summer. *J. Clim.* 12 (5), 1353–1367.

Sun, J., Wang, H., Wei, J., and Qin, L. (2016). The Sources and Transportation of Water Vapor in Persistent Heavy Rainfall Events in the Yangze-Huaihe River Valley. *Acta Meteorologica Sinica* 74 (4), 542–555.

Sun, J., Wei, J., Fu, S., Zhang, Y., and Wang, H. (2018). The Multi-Scale Physical Model for Persistent Heavy Rainfall Events in the Yangtze-Huaihe River valley. *Chin. J. Atmos. Sci.* 42 (4), 741–754. doi:10.3878/j.issn.1006-9895.1803.17246 (in Chinese).

Takaya, K., and Nakamura, H. (2001). A Formulation of a Phase-independent Wave-Activity Flux for Stationary and Migratory Quasigeostrophic Eddies on a Zonally Varying Basic Flow. *J. Atmos. Sci.* 58 (6), 608–627. doi:10.1175/1520-0469(2001)058<0608:afoapi>2.0.co;2

Tam, C.-Y., and Li, T. (2006). The Origin and Dispersion Characteristics of the Observed Tropical Summertime Synoptic-Scale Waves over the Western Pacific*. *Monthly Weather Rev.* 134 (6), 1630–1646. doi:10.1175/mwr3147.1

Tao, S., and Chen, L. (1987). *A Review of Recent Research on the East Asian Summer Monsoon in China*. Monsoon Meteorology.

Wang, C., Yao, S., Huang, A., and Gao, Q. (2021). Numerical Simulation of Effects of Synoptic Scale Disturbances at Different Latitudes on Meiyu Precipitation in 2020. *Trans. Atmos. Sci.* doi:10.13878/j.cnki.dqkxxb.20201122001 (in Chinese).

Wang, H., Sun, J., Wei, J., and Zhao, S. (2014). Classification of Persistent Heavy Rainfall Events over Southern China during Recent 30 Years. *Climatic Environ. Res.* 19 (6), 713–725. (in Chinese).

Wang, Z., Yang, S., Lau, N.-C., and Duan, A. (2018). Teleconnection between Summer NAO and East China Rainfall Variations: A Bridge Effect of the Tibetan Plateau. *J. Clim.* 31, 6433–6444. doi:10.1175/JCLI-D-17-0413.1

Weng, H., Xue, L. K., and Xue, Y. (2008). Multi-scale Summer Rainfall Variability over china and its Long-Term Link to Global Sea Surface Temperature Variability. *J. Meteorol. Soc. Jpn.* 77 (4), 845–857.

Xue, F., Wang, H., and He, J. (2003). Interannual Variability of Mascarene High and Australian High and Their Influences on Summer Rainfall over East Asia. *Chin.Sci.Bull.* 48, 492–497. doi:10.1007/BF03183258

Yan, X., Yang, S., Wang, T., Maloney, E. D., Dong, S., Wei, W., et al. (2019). Quasi-biweekly Oscillation of the Asian Monsoon Rainfall in Late Summer and Autumn: Different Types of Structure and Propagation. *Clim. Dyn.* 53, 6611–6628. doi:10.1007/s00382-019-04946-3

Yang, J., Wang, B., Wang, B., and Bao, Q. (2010). Biweekly and 21-30-day Variations of the Subtropical Summer Monsoon Rainfall over the Lower Reach of the Yangtze River basin. *J. Clim.* 23 (5), 1146–1159. doi:10.1175/2009JCLI3005.1

Yang, Q. (2009). The 20-30-day Oscillation of the Global Circulation and Heavy Precipitation over the Lower Reaches of the Yangtze River valley. *Sci. China Ser. D-earth Sci.* 52, 1485–1501. doi:10.1007/s11430-009-0156-2

Yao, S., and Huang, Q. (2016). An Analysis of Extreme Intraseasonal Rainfall Events during January-March 2010 over Eastern China. *Dyn. Atmospheres Oceans* 75, 22–32. doi:10.1016/j.dynatmoce.2016.04.001

Yao, S., Huang, Q., Zhang, Y., and Kuang, X. (2012). A Study on Response of Precipitation in China to Monsoon Intraseasonal Oscillation. *J. Trop. Meteorology* 18, 503–511.

Yao, S., Tong, Q., Li, T., and Gong, K. (2019). The 10-30-day Oscillation of winter Rainfall in Southern China and its Relationship with Circulation Patterns in Different Latitudes. *Int. J. Climatol* 40 (1), 3268–3280. doi:10.1002/joc.6396

Yihui, D., and Zunya, W. (2008). A Study of Rainy Seasons in China. *Meteorol. Atmos. Phys.* 100 (1-4), 121–138. doi:10.1007/s00703-008-0299-2

Yin, Z., Zhu, L., and Yuan, D. (2014). The North-south Anti-phase Distribution of Rainfall in Meiyu Periods and its Relationship with Quasi-Biweekly Oscillation in the Atmosphere. *J. Trop. Meteorology* 20, 154–162.

Yuan, Y., Gao, H., Li, W., Liu, Y., Chen, L., Zhou, B., et al. (2017). The 2016 Summer Floods in china and Associated Physical Mechanisms: a Comparison with 1998. *J. Meteorol. Res.* 31, 261–277. doi:10.1007/s13351-017-6192-5

Zhai, P., Sun, A., Ren, F., Liu, X., Gao, B., and Zhang, Q. (1999). Changes of Climate Extremes in China. *Climatic Change* 42 (1), 203–218. doi:10.1007/978-94-015-9265-9_13

Zhang, R. (2001). Relations of Water Vapor Transport from Indian Monsoon with that over East Asia and the Summer Rainfall in China. *Adv. Atmos. Sci.* 18 (5), 1005–1017.

Zhang, S., Tao, S., Zhang, Q., and Wei, J. (2002). Large and Meso-? Scale Characteristics of Intense Rainfall in the Mid- and Lower Reaches of the Yangtze River. *Chin. Sci Bull* 47 (9), 779–786. doi:10.1360/02tb9176

Zhang, Z., Sun, X., and Yang, X.-Q. (2018). Understanding the Interdecadal Variability of East Asian Summer Monsoon Precipitation: Joint Influence of Three Oceanic Signals. *J. Clim.* 31, 5485–5506. doi:10.1175/JCLI-D-17-0657.1

Zhu, C., Nakazawa, T., Li, J., and Chen, L. (2003). The 30-60 Day Intraseasonal Oscillation over the Western North Pacific Ocean and its Impacts on Summer Flooding in China during 1998. *Geophys. Res. Lett.* 30 (18), 1952. doi:10.1029/2003GL017817

Zong, H., and Wu, L. (2015). Re-examination of Tropical Cyclone Formation in Monsoon Troughs over the Western North Pacific. *Adv. Atmos. Sci.* 32, 924–934. doi:10.1007/s00376-014-4115-2

Conflict of Interest: The authors declare that the research was conducted in the absence of any commercial or financial relationships that could be construed as a potential conflict of interest.